J Mater Sci (2011) 46:3792–3801
DOI 10.1007/s10853-011-5293-2

Vertically aligned nanocrystalline Cu–ZnO thin films for photoelectrochemical splitting of water

Vidhika Sharma · Pushpendra Kumar · Jaya Shrivastava · Anjana Solanki · V. R. Satsangi · Sahab Dass · Rohit Shrivastav

Received: 23 October 2010 / Accepted: 14 January 2011 / Published online: 26 January 2011

Abstract Cu-incorporated nanocrystalline ZnO thin films were deposited on glass substrate by sol–gel. To a solution of zinc acetate 2-hydrate in dimethyl formamide, calculated quantities of copper acetate were added. The clear solution, obtained after 2 h of continuous stirring, was coated on ITO plates. Pre-annealing at 250 °C was followed by sintering at 400, 500, and 600 °C. XRD analysis revealed dominant evolution of hexagonal ZnO with a possible simultaneous growth of meta-stable cubic ZnO. AFM and SEM analysis indicated preferential growth of nanocrystallites along *c*-axis. Optical characterization led to two prominent absorption thresholds in the UV region; one matching with the band gap of bulk ZnO and the second at slightly higher energy, suggesting quantum confinement effect in nanocrystallites. Cu incorporation influenced the two band gap energies differently. Photoelectrochemical splitting of water using 1% at. Cu–ZnO film sintered at 600 °C resulted in 141% gain in photocurrent at zero bias.

Introduction

Dwindling availability of fossil fuels, their increasing cost, and heavy emission of polluting gases on their burning have compelled researchers to look for alternate and clean sources of energy. Hence, use of transition metal oxides for photoelectrochemical (PEC) splitting of water to produce hydrogen, a valuable fuel, is being hotly pursued [1–7]. In such investigations, TiO_2 has often been used as photoelectrode. ZnO, having almost similar band gap and band edge energetic, is seen by some researchers as better alternative to TiO_2. The main reasons for growing interest in ZnO for this application are its direct band gap, relatively high electron mobility, and very unique defect chemistry, which allow tuning its structural and optical features [8]. Although the stability of ZnO in aqueous PEC environment under anodic bias has been doubted by some workers [9]. Yet, there are reports to suggest that ZnO can yield almost stabilized PEC photocurrent for long durations [10]. In order to reach higher absorption coefficient in ZnO, especially under visible light irradiation, its band gap reduction by impurity doping may be attempted. Theoretical studies have shown that Group IB elements (Cu, Ag, and Au) can favorably lead to band gap-reduced ZnO [11]. Among above choices, Cu is the best on account of the comparable atomic radii of Cu and Zn atoms leading to the lowest formation energy [12].

ZnO dominantly exists as hexagonal wurtzite structure with the lattice parameters: $c = 5.205$ Å, $a = 3.249$ Å. Its native n-type semiconductor behavior is originated by the existence of Zn interstitials and oxygen vacancies in the lattice [13]. Cu-doped ZnO has been studied in recent years mainly for electrical and ferromagnetic properties [14]. Solubility of copper in ZnO lattice is around 1 mol%, and it can effectively substitute Zn^{2+} ions. Room temperature Cu doping of ZnO results in reduced number of carriers. With the existence of donor–acceptor associate for Cu_{Zn}, where $Cu^{\bullet}_{Zn} + Zn^{\bullet}_{i} \rightarrow [Cu_{Zn} + Zn_i]^x$, the ionization of such deep neutral defects requires high energy ($\sim$3.0 eV), and

V. Sharma · P. Kumar · J. Shrivastava · A. Solanki · S. Dass · R. Shrivastav (✉)
Department of Chemistry, Dayalbagh Educational Institute, Dayalbagh, Agra 282110, India
e-mail: rohitshrivastav_dei@yahoo.co.in

V. R. Satsangi
Department of Physics and Computer Science, Dayalbagh Educational Institute, Dayalbagh, Agra 282110, India

the presence of such complex defects compensates for the n-type conductivity of ZnO [15, 16]. Many workers investigated structural and optical properties of Cu-doped ZnO, but, their observations are varied. While, in some studies, the band gap was reduced on Cu doping, in few reports band broadening is also mentioned. Cu doping can lead to the generation of relatively uncommon p-type ZnO also [17].

Sol–gel synthesis continues to be the most convenient and low-cost method for the synthesis of transition metal-doped ZnO. However, in this process, the oxidation/spin state, homogeneity, and substitutional placement of the incorporated metal are important considerations. In general, some alcoholic solvents, viz., ethanol, propanol, and methoxy ethanol are used in this synthesis, as these also participate as reactant [18–20]. In such methods, heating at 60–100 °C is needed to dissolve the precursor, besides adding lactic acid to impart stability/homogeneity to the sol and prevent the occurrence of hydrolysis/precipitation reaction. Under such reaction conditions, the alteration in the oxidation state of the incorporated metal cannot be ruled out [21]. This demands milder reaction conditions.

This study deals with the synthesis, characterization, and PEC application of Cu-incorporated ZnO films. Films were prepared by sol–gel using dimethyl formamide (DMF), which being a highly polar solvent was able to dissolve zinc acetate precursor and copper salt even at room temperature (<35 °C). Further, the relatively low vapor pressure of DMF was helpful in preventing premature and uneven drying, which may otherwise cause cracking and disrupt ordered crystallisation in the films. The study is primarily aimed to evaluate the effect of Cu incorporation (1–7% at.) on the microstructure and optical properties of nanostructured ZnO thin films, especially from the view point of application in PEC splitting of water.

Experimental

ZnO thin films preparation

Zinc acetate 2-hydrate (ZAD) was dissolved in DMF along with calculated amount of copper acetate under continuous stirring. The content was further stirred for 2 h to obtain a clear solution, which was spin coated on conducting glass (ITO) substrate (3 × 2 cm) at 7500 rpm. After each coat, deposited film was dried at 50 °C for 5 min. Finally, it was pre-annealed at 250 °C for 2 h, and then annealed in air at temperatures 400, 500, and 600 °C for 2 h. Films were deposited on nearly 3/4th length of substrate plate, and the uncovered area was used to establish electrical contact.

Characterization

X-ray diffraction pattern of samples was recorded by glancing angle X-ray diffractometer (Bruker AXS D8 Advance, Germany), equipped with graphite monochromator, a mirror at a fixed incidence angle of 1°–5° and Cu Kα as the radiation source. The angular accuracy was 0.001°, and the angular resolution was better than 0.01°. Utilizing the X-ray diffraction data and equation, $t = k\lambda/B\mathrm{Cos}\theta$, Scherrer's calculations were attempted to estimate average crystallite size in the samples, where t is crystallite size, B the full width at half maxima, and λ the wavelength of X-ray used (1.548 Å). Utilizing equations, $\delta = 1/t^2$ and $\varepsilon = B\mathrm{Cos}\theta/4$, the dislocation density (δ) and the micro-strain (ε) in the films were also estimated [22].

Scanning Electron micrographs (SEMs) of samples were recorded using JEOL JSMS 800 LV. Surface topographic images of the films were taken by employing Atomic Force Microscope (Nanosurf Easy-Scan, Switzerland; Version 1.8). The set point force was fixed at 20 μN for all the images, which were obtained for 256 × 256 data points for each scan size 5 × 5 μm. Absorption spectra of ZnO films (recorded with respect to the bare substrate by employing double beam UV–vis spectrophotometer, UV-2450, Shimadzu, in the range 360–760 nm) were analyzed by plotting $(\alpha h\upsilon)^2$ versus $h\upsilon$, based on Eq. 1 [23],

$$\alpha h\upsilon = A(h\upsilon - E_g)^{n/2} \quad (1)$$

where α is absorption coefficient, A is a constant (independent from frequency υ), and n the exponent that depends upon the quantum selection rules for the particular material. The intercept of the straight line portion of $(\alpha h\upsilon)^2$ versus photon-energy ($h\upsilon$) plot on $h\upsilon$ axis yielded optical band gap (E_g) for direct allowed transition ($n = 1$).

Flat band potential (V_{fb}) and charge carrier density (N_D) are important physical properties of the semiconductors from their PEC application view point. These were determined by measuring the capacitance (C) of the electrode–electrolyte interface at different electrode potentials (V) and using Eqs. 2 and 3 [24],

$$1/C^2 = [2/\varepsilon_o\varepsilon_s qN_D]\,[V - V_{fb} - (k_B T/q), \quad (2)$$

$$S = 2/(\varepsilon_o\varepsilon_s qN_D), \quad (3)$$

where ε_0 and ε_s are permittivity of free space and ZnO, respectively, q the electronic charge, T the temperature in Kelvin, k_B the Boltzmann's constant, and S the slope of $1/C^2$ versus V, i.e., Mott–Schottky (MS) curve. In this study, by employing LCR meter (Agilent Technology Model 4263B), and using aqueous solution of NaOH (0.1 M, pH 12) as the electrolyte, the capacitance at ZnO–solution junction was measured, with V varying from −1500 to 1500 mV, at 1 kHz signal frequency. The intercepts of

linear portion of the MS curves on the potential axis yielded the values of V_{fb}, while N_D values were determined from slope.

PEC measurements

ZnO films were used as working electrode (WE) for PEC splitting of water, for which an Ohmic electrical contact was created from the uncovered area of the substrate (where films were not deposited) with silver paint and a copper wire. Excluding an area of 2.25 cm^2 (1.5 × 1.5 cm) at the center of the film, all edges and the electrical contact were sealed by non-transparent, non-conducting epoxy resin, Hysol (Dexter Singapore). PEC studies were conducted using platinum foil counter electrode (CE) and saturated calomel reference electrode (SCE) in an electrochemical cell, having a Pyrex window for incoming radiations and a water jacket around it, to prevent heating. Aqueous solution of NaOH (0.1 M, pH 12), purged with N_2 for 15–20 min just before PEC measurement was used as electrolyte. Potentiostat (Model ECDA 001, Conserv Enterprises, Mumbai) and 150W Xenon Arc Lamp (Oriel, USA, used as light source) were employed to record current–voltage (*I–V*) characteristics of the cell, both under darkness and illumination. Reagents with purity >99.9% and double distilled deionized water (specific conductance $< 10^{-6}$ mho cm^{-1}) were used throughout. Film samples were prepared in triplicate, and with each sample 3–5 repetitive measurements were recorded during the span of 3–5 months. Results are reproducible within ±15% deviation and clearly suggest that not only the ZnO films are stable in PEC cell, but even the evolved nanostructure in films possibly remains intact for long durations.

Results and discussion

Chemical reaction for Zn in the used preparation method may be tentatively written as:

$$Zn(CH_3COO)_2{\cdot}2H_2O \rightarrow Zn(CH_3COO)_2 + 2H_2O$$

$$Zn(CH_3COO)_2 + 2HCON(CH_3)_2 \rightarrow Zn\left[CON(CH_3)_2\right] + 2CH_3COOH$$

$$Zn\left[CON(CH_3)_2\right] + 2H_2O \rightarrow Zn(OH)_2 + 2HCON(CH_3)_2$$

$$Zn(OH)_2 \rightarrow ZnO + H_2O$$

Prepared samples of ZnO films were of n-type, suggesting O vacancy and/or Zn interstitials, due to possible non-stoichiometric growth [25]. Resistivity of films decreased with increase in sintering temperature. Further, it decreased sharply (nearly by an order) on Cu incorporation and continued to decrease with increase in Cu concentration, except in 7% at. Cu-incorporated samples sintered at 400 and 500 °C, where it has again increased marginally. Measured density of films varied from 3.26 to 4.45 g cm^{-3}, which is ≈58–79% the of theoretical bulk density (5.60 g cm^{-3}) of ZnO (Table 1), suggesting that the films are porous and can provide a large contact area with electrolyte, when used in PEC cell. Slight increase in density with rise in sintering temperature may be attributed to the possible coalescing of grains at higher temperature. Cu incorporation led to significant fall in density suggesting opening up of the lattice, also evident from the significant increase in microstrain and dislocation density (Table 2) on Cu incorporation. The variation in density can be understood in the light of the crystallization process in the system, which is temperature dependent [26].

Figure 1 shows glancing angle X-ray diffraction patterns (before and after copper incorporation) of zinc oxide films sintered at 400, 500, and 600 °C. The presence of multiple peaks of the ZnO phase indicates the polycrystalline nature of films [27]. In earlier studies, ZnO films obtained by molecular beam RF sputtering and sol–gel were also reported to be polycrystalline [28, 29]. The high intensity peaks at 2θ angles 35.3°, 37.7°, and 42.2°, besides several other low intensity peaks, can be easily ascribed to the underlying SnO_2:In layer on the substrate. However, the additionally emerged peaks in Cu–ZnO films at 2θ angles 31.8°, 34.4°, and 36.2° correspond to diffraction from planes (100), (002), and (101), respectively, of hexagonal wurtzite ZnO (JCPDS, Card. 89-1397). It can also be observed that the substrate peaks at 37.7 and 42.2° exhibit

Table 1 Observed values of density and electrical resistivity of ZnO/Cu–ZnO films

Sintering temperature (°C)	Incorporated concentration of Cu (% at.)	Density (g cm^{-3})	Electrical resistivity (kΩ cm)
400	–	4.35	1.35
400	1	3.26	0.98
400	3	3.34	0.67
400	5	3.37	0.77
400	7	3.36	1.03
500	–	4.37	1.13
500	1	3.30	0.64
500	3	3.37	0.65
500	5	3.53	0.50
500	7	3.60	0.72
600	–	4.45	1.01
600	1	3.33	0.75
600	3	3.61	0.63
600	5	3.68	0.46
600	7	3.68	0.45

Table 2 Microstructural quantities of ZnO/Cu–ZnO films

Sintering temperature (°C)	Incorporated concentration of Cu (% at.)	Average crystallite size (nm)	[Dislocation density (δ)] $\times 10^{-14}$ (line^2/m$^{2)}$	Microstrain (ε) 10^{-3}	RMS surface roughness (nm)
400	–	43	5.4	0.73	09
400	1	29	12.7	0.95	10
400	3	24	17.3	1.23	10
400	5	20	27.7	1.53	15
400	7	23	20.6	1.06	09
500	–	32	9.7	0.97	10
500	1	28	13.7	0.98	10
500	3	29	11.8	1.06	13
500	5	26	14.7	1.26	15
500	7	20	27.7	1.56	12
600	–	29	12.7	1.08	07
600	1	23	20.6	1.21	11
600	3	31	10.4	1.22	08
600	5	25	17.3	1.43	06
600	7	31	11.1	1.33	12

significant increase in intensity on ZnO film deposition. This may be attributed to the evolution of metastable phase cubic zincblend ZnO also in the samples corresponding to which diffraction peaks at 2θ angles 37.2° and 42.2° from (111) and (200) planes (JCPDS, Card 65-0682) are probably overlapped by the substrate peaks. The existence of oxides of copper as distinct phase is not seen. With increase in incorporated concentration of Cu, crystallites of finer dimensions evolved. This is particularly evident in samples sintered at 600 °C. With rise in sintering temperature, the crystallinity decreased [30]. The attempts to grow Cu–ZnO films on ordinary glass plates to eliminate the appearance of substrate peaks in the XRD pattern resulted only in an amorphous structure. This suggests that ITO coating on glass plate also probably plays some role in further growth of ZnO film over it. More work is desired in this direction.

Thermodynamically ZnO is stable with the wurtzite phase due to its ionicity that resides exactly at the borderline between the covalent and the ionic materials. However, the total energy of wurtzite ZnO is lower than that of zincblend phase only by 50 meV, suggesting that the metastable zincblend ZnO can also evolve. In fact, evolution of zincblend ZnO by sol–gel process is reported even earlier [31]. In several studies *c*-axis oriented growth of wurtzite ZnO grains is seen [32]. The relative intensities of the peaks in the XRD pattern, in this study also, suggest some grain orientation perpendicular to the substrate in the samples [33].

SEM and AFM images (Fig. 2, 3, 4, and 5) reveal homogeneous and continuous growth in films. Separate coating layers are not visible, but partial grain orientation in the preferred *c*-axis can be seen. In films sintered at 500 °C, vertical growth of nanocrystallites is most prominent. AFM data were utilized to estimate root-mean-square (RMS) surface roughness and the values indicate increased roughness in films sintered at 500 °C compared to films sintered at 400 °C (Table 2). However, with sintering at 600 °C, a partial smoothing in the surface can be seen. In Cu-incorporated films, most prominent vertical growth of crystallites occurred in samples sintered at 400 and 500 °C.

Optical UV–vis absorption spectra of ZnO/Cu–ZnO thin films from 300 to 700 nm (Fig. 6) indicate that the absorption is relatively more in films sintered at higher temperatures. In general, the decrease in optical absorption can be attributed to the improvement in crystallinity and stoichiometry. From XRD analysis, the maximum crystallinity is seen in films sintered at 400 °C, while films sintered at 600 °C have the lowest crystallinity. The absorption pattern is thus, guided both by variations in crystallinity and stoichiometry. The absorption spectra of films present an interesting observation, where, apart from defects induced some low intensity absorptions corresponding to *d*–*d* transitions in the visible region, a board absorption band with two prominent absorption thresholds can be seen in the UV region. The first one at around 400 nm may be due to the onset of fundamental absorption corresponding to O:2*p* → Zn:4*s* charge-transfer band, widely reported in literature for ZnO. Corresponding to this threshold, band gap (E_g) values were determined by plotting $(\alpha h\upsilon)^2$ versus ($h\upsilon$) (Fig. 7). The values (Table 3) are close to the reported value for bulk ZnO, and there are only marginal changes in it even after Cu incorporation. The existence of an additional absorption threshold at

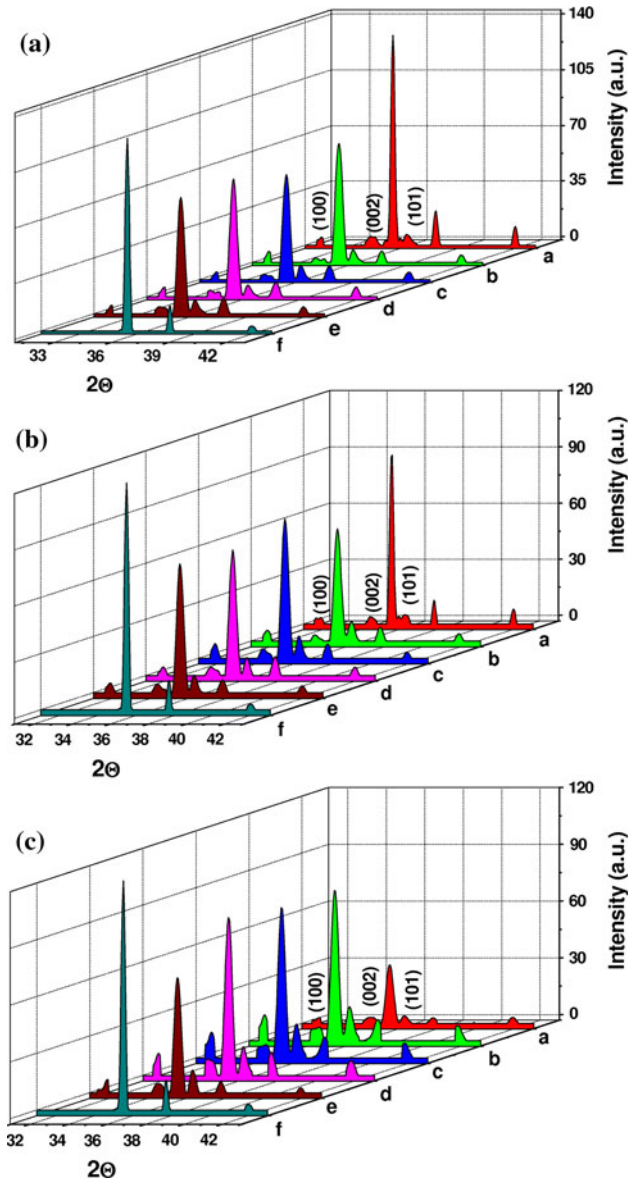

Fig. 1 X-ray diffraction pattern of ZnO and Cu–ZnO films. Sintering temperature: 400 °C (**a**), 500 °C (**b**), and 600 °C (**c**); Incorporated concentration of Cu: nil (*a*), 1 (*b*), 3 (*c*), 5 (*d*), and 7% at. (*e*); Diffraction pattern from ITO substrate (*f*), peaks corresponding to wurtzite ZnO

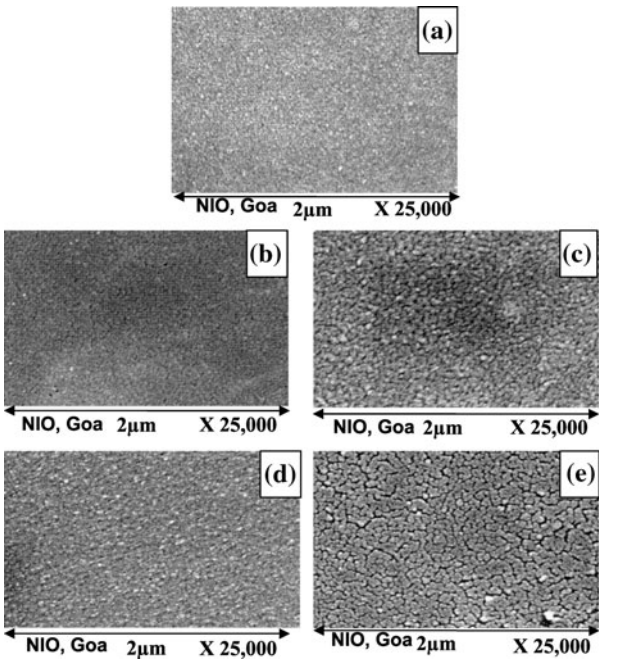

Fig. 2 SEM images of ZnO and Cu–ZnO films. Sintering temperature: 600 °C; incorporated concentration of Cu: nil (**a**), 1 (**b**), 3 (**c**), 5 (**d**), and 7% at. (**e**)

even lower wavelength, probably, indicates particle/grain size heterogeneity in the samples lying in a range where a fraction of particles/grains are of very low grain size and, possibly due to quantum confinement, this fraction shows band gap higher than that of bulk system [34, 35]. Band gap values corresponding to this threshold (presented in parenthesis in Table 3) show marked change on Cu incorporation, although the variation is up and down and trend is not clear. Probably, band gap energies in very low size range of nanoparticles, to which this absorption threshold seemingly corresponds, also depends upon nanoparticles morphology. More work is needed to understand this aspect.

In PEC cell measurements, the observed current–potential (*I–V*) curves demonstrate n-type nature of ZnO films [16]. Table 4 depicts the open circuit voltage (V_{oc}) and short circuit current (J_{sc}), recorded under illumination. The V_{oc} values are comparable to the values reported earlier [36]. There is significant change in J_{sc} on Cu incorporation, and highest J_{sc} was recorded with 1% at. Cu–ZnO films sintered at 600 °C. The observed variation in photocurrent density (i.e., $I_{illumination} - I_{darkness}$) with applied voltage is shown in Fig. 8. Films sintered at 600 °C yield maximum photocurrent, but the photoresponse of films sintered at 400 °C is very poor. Since, there is no additional redox couple in the electrolyte, the significant value of photocurrent density can be attributed to electrochemical splitting of water, which was well indicated by evolution of gases in the form of bubbles on the electrode surface. The photocurrent density is altered significantly by copper incorporation. It was maximum when 1% at. Cu–ZnO film sintered at 600 °C was used as WE. Cu–ZnO films, prepared in this study, can efficiently absorb UV light, showing, at the same time, moderate to low absorption in the visible region. Further, in this case, band edges are seemingly well aligned to redox levels corresponding to hydrogen and oxygen evolution, which is indicated by significant short circuit current, especially with films sintered at 500 and 600 °C. PEC data were further utilized to evaluate applied bias photon-to-current efficiency (ABPE)

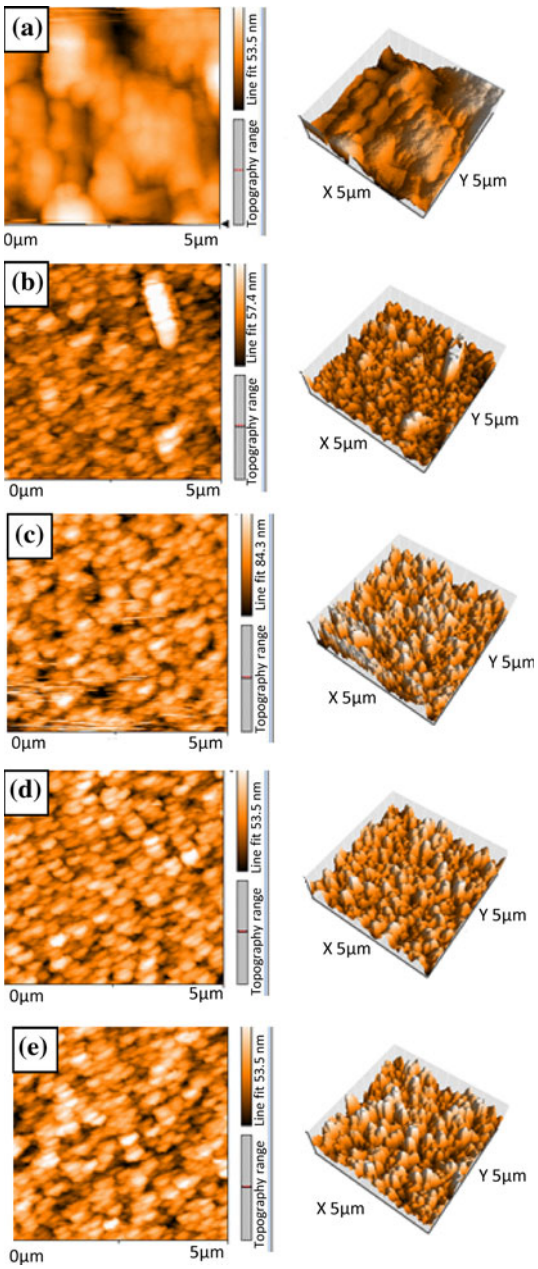

Fig. 3 AFM images of ZnO and Cu–ZnO films. Sintering temperature: 400 °C; incorporated concentration of Cu: nil (**a**), 1 (**b**), 3 (**c**), 5 (**d**), and 7% at. (**e**)

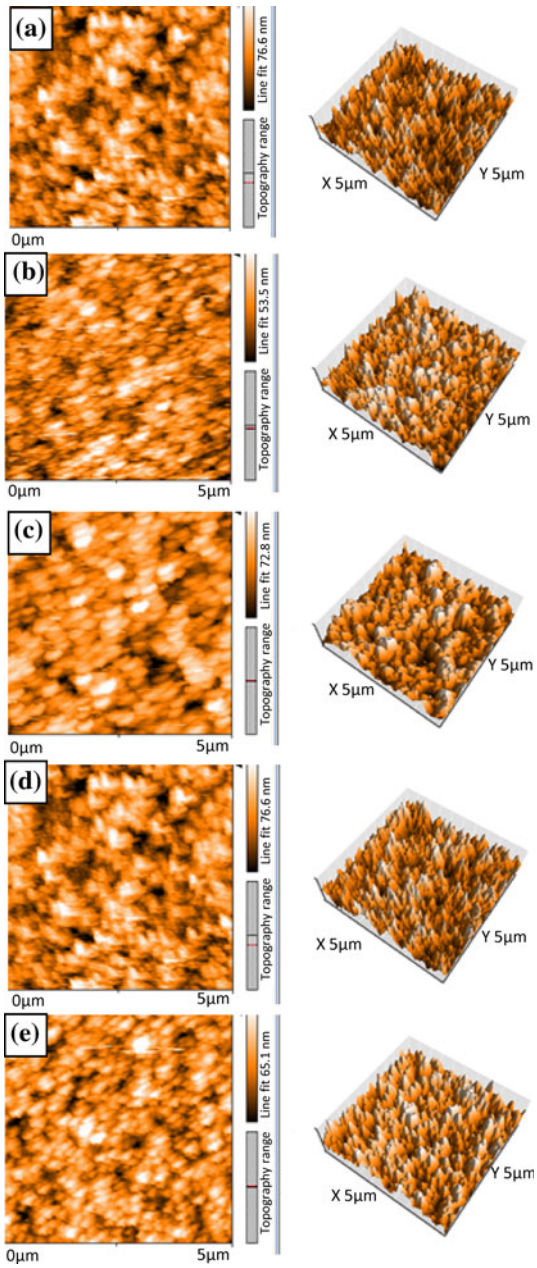

Fig. 4 AFM images of ZnO and Cu–ZnO films. Sintering temperature: 500 °C; incorporated concentration of Cu: nil (**a**), 1 (**b**), 3 (**c**), 5 (**d**), and 7% at. (**e**)

of the cell under 500 mV bias [2]. The values, presented in Table 4, once again suggest that the photoresponse is maximum for 1% Cu-incorporated films and increases with the rise in sintering temperature.

The values of V_{fb} derived from MS plots (Table 3) are comparable to the values reported in some earlier studies for ZnO [25]. Further, V_{fb} values are different from "Onset potentials", obtained from I^2 versus V relations, suggesting the presence of surface states at the electrode–electrolyte interface, where carriers may recombine easily [37]. The typical maximum charge carrier density reported for the zincblend ZnO is $\sim 10^{19}$ cm^{-3}, while for the wurtzite ZnO is $\sim 10^{20}$ cm^{-3}, which means it is an order of magnitude higher in the wurtzite ZnO [25]. The measured carrier density in all the samples (ZnO and Cu–ZnO) prepared in this study, as determined from the slope of MS curves are in the expected range (Table 3). Cu incorporation in ZnO, in general, resulted in an increase in charge carrier density. However, in some samples, the values have decreased (reason not clear at present). For PEC application and

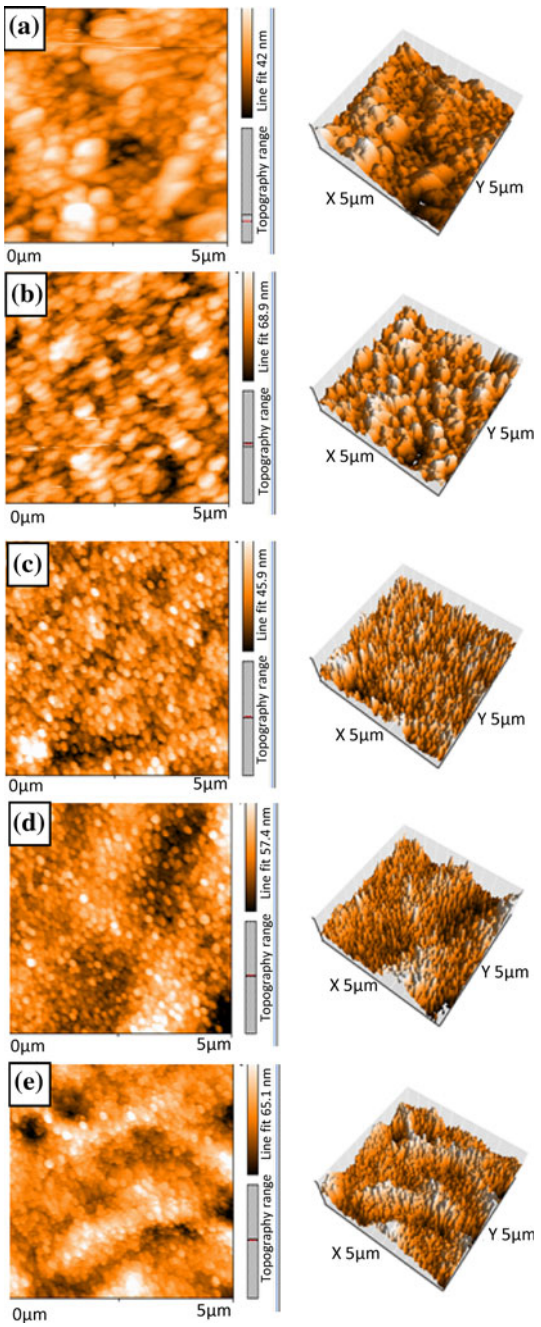

Fig. 5 AFM images of ZnO and Cu–ZnO films. Sintering temperature: 600 °C; incorporated concentration of Cu: nil (**a**), 1 (**b**), 3 (**c**), 5 (**d**) and 7% at. (**e**)

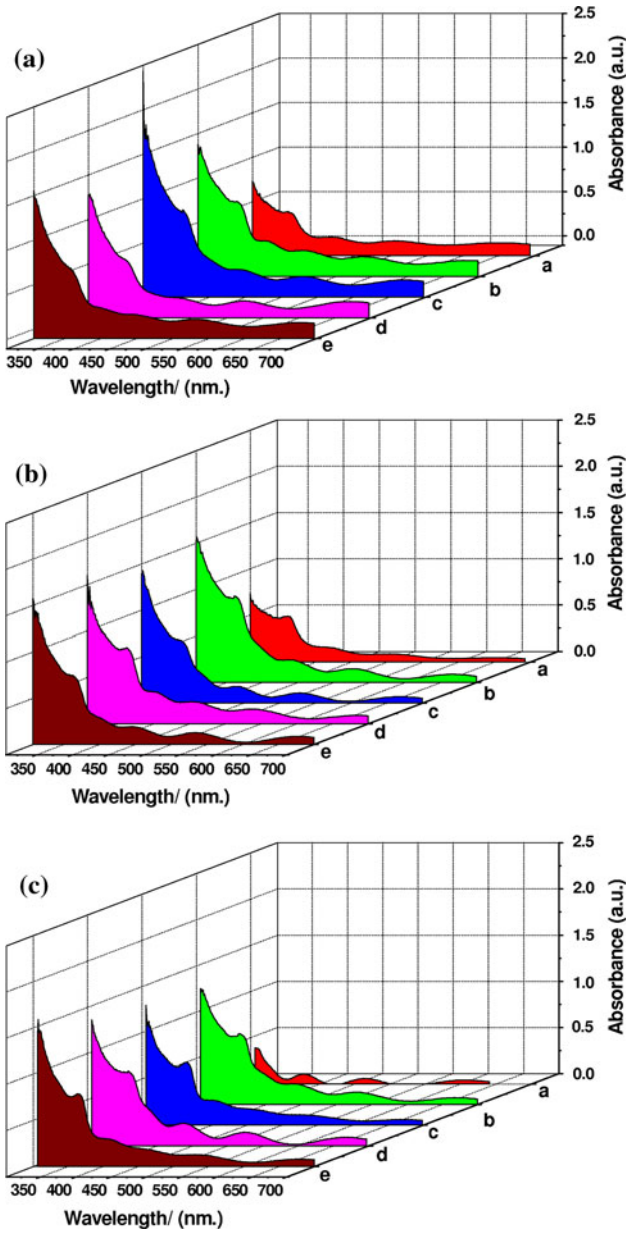

Fig. 6 Absorbance versus wavelength plots for ZnO and Cu–ZnO films. Sintering temperature: 400 °C (**a**), 500 °C (**b**), and 600 °C (**c**); Incorporated concentration of Cu: nil (*a*), 1 (*b*), 3 (*c*), 5 (*d*), and 7% at. (*e*)

current generation, apart from the concentration of carrier, their mobility is also important. Measured resistivity of thin films, being low in the samples sintered at 500 and 600 °C, suggest higher carrier mobility. Copper incorporation has also led to significant fall in resistivity. Thus, the high photocurrent values recorded with samples sintered at 500 and 600 °C, especially with 1% at. Cu–ZnO, may be due to improved optical absorption coupled with decreased resistivity, and carrier mobility appears more critical than carrier concentration for PEC application. Yet, there is no direct evidence to suggest that nanostructured Cu–ZnO is better than the bulk system for PEC splitting of water, as expected improvement in the light absorption in nanosystem, due to increased surface area, gets nullified by a significant blue shift in the absorption threshold. Thus, size optimization is crucial in the whole process.

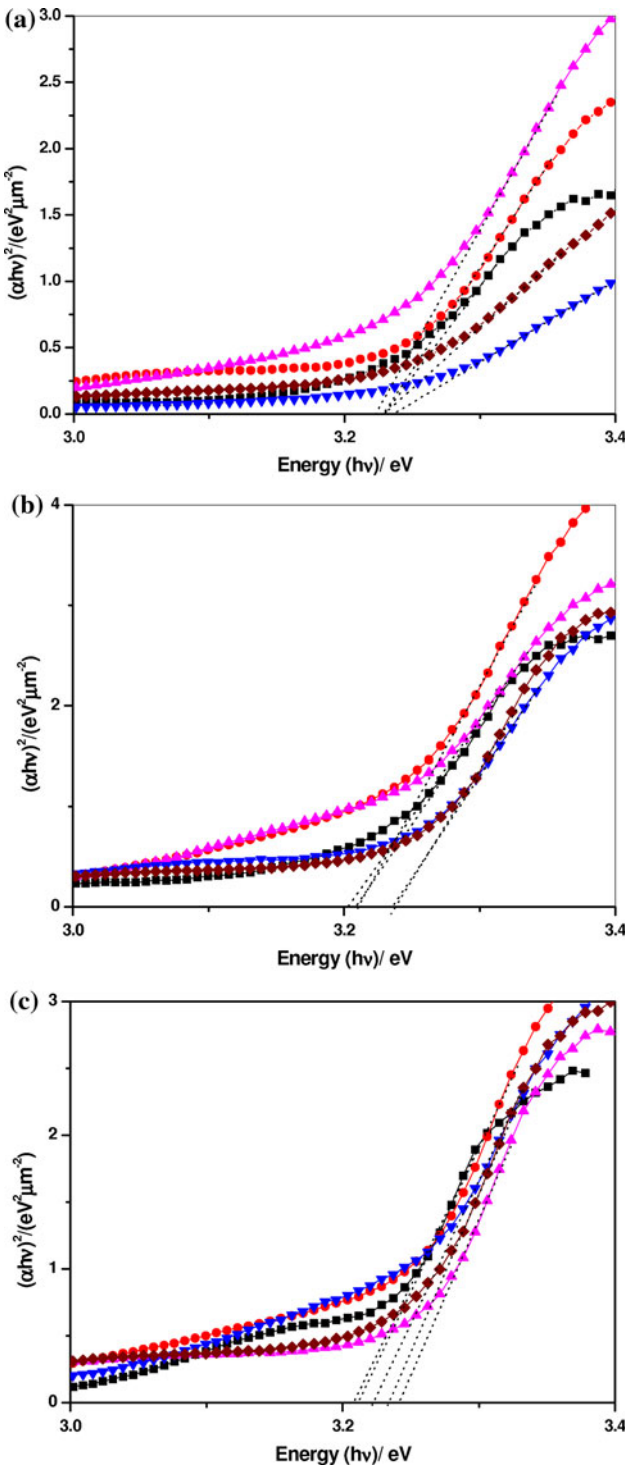

Fig. 7 $(\alpha h\upsilon)^2$ versus $h\upsilon$ plots for ZnO and Cu–ZnO films. Sintering temperature: 400 °C (**a**), 500 °C (**b**), and 600 °C (**c**); Incorporated concentration of Cu: nil (*filled square*), 1 (*filled circle*), 3 (*filled triangle*), 5 (*filled inverted triangle*), and 7% at. (*filled diamond*)

Conclusions

This study, thus, leads to the following conclusions: (i) Evolution of hexagonal wurtzite with the possible concomitant growth of cubic zincblend ZnO has been obtained by the preparatory method. (ii) Observed absorption spectra and the optical band gap of the films suggest that the films are efficient UV absorber and moderate weak absorber of visible light. Thus, their use for PEC splitting of water is possible. Further, due to quantum

Table 3 Values of Band gap energy (E_g), Flat band potential (V_{fb}), and Charge carrier density (N_D) for ZnO/Cu–ZnO films

Sintering temperature (°C)	Incorporated concentration of Cu (% at.)	E_g (eV)	V_{fb} (V)	$N_D \times 10^{-21}$ (cm^{-3})
400	–	3.22 (3.56)	−0.58	0.38
400	1	3.22 (3.43)	−0.74	0.53
400	3	3.22 (3.62)	−0.77	0.16
400	5	3.23 (3.36)	−0.74	0.33
400	7	3.24 (3.35)	−0.69	0.67
500	–	3.21 (3.44)	−0.64	0.13
500	1	3.20 (3.31)	−0.73	0.80
500	3	3.22 (3.56)	−0.87	0.18
500	5	3.21 (3.63)	−0.72	0.53
500	7	3.22 (3.25)	−0.66	0.25
600	–	3.22 (3.63)	−0.76	0.67
600	1	3.22 (3.41)	−0.85	0.67
600	3	3.21 (3.78)	−0.87	1.51
600	5	3.23 (3.55)	−0.75	1.34
600	7	3.24 (3.55)	−0.72	0.44

E_g values in parenthesis correspond to the additional absorption threshold observed at lower λ in UV region (refer to the text)

Table 4 Observed values of open circuit potential (V_{oc}) and short circuit current (J_{sc}) on using Cu–ZnO films of ZnO as working electrode in PEC cell under illumination

Sintering temperature (°C)	Incorporated concentration of Cu (% at.)	V_{oc} (V)	J_{sc} ($\mu A\ cm^{-2}$)	Applied bias photon-to-current efficiency (ABPE)
400	–	0.50	19	0.07
400	1	0.76	413	0.38
400	3	0.64	109	0.10
400	5	0.47	70	0.05
400	7	0.49	117	0.13
500	–	0.71	216	0.25
500	1	0.67	427	0.45
500	3	0.53	180	0.23
500	5	0.48	150	0.16
500	7	0.47	209	0.16
600	–	0.69	312	0.79
600	1	0.69	752	0.66
600	3	0.50	169	0.20
600	5	0.48	255	0.45
600	7	0.43	154	0.13

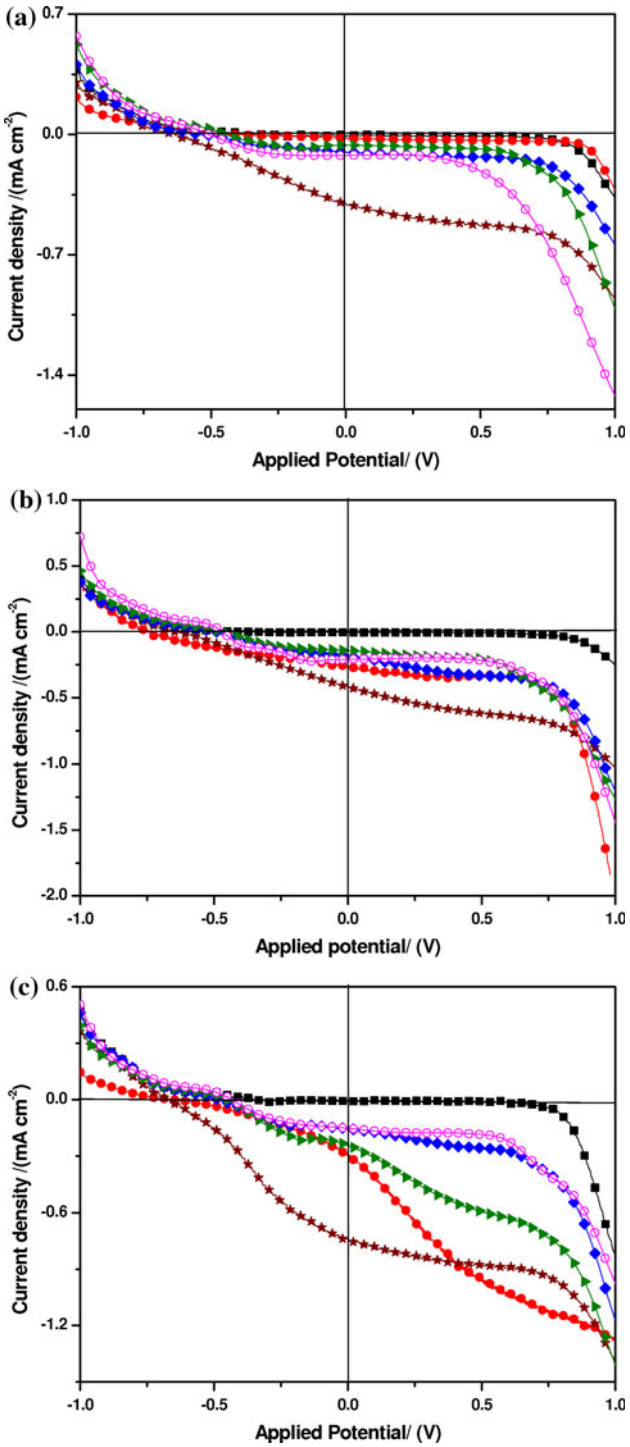

Fig. 8 Variation in photocurrent density with applied potential employing ZnO and Cu–ZnO films as working electrode. Sintering temperature: 400 °C (**a**), 500 °C (**b**), and 600 °C (**c**); Incorporated concentration of Cu: nil (*filled circle*), 1 (*filled star*), 3 (*filled diamond*), 5 (*filled triangle*), and 7% at. (*open circle*)

confinement effect, two absorption thresholds are seen in the UV region with corresponding band gap energies getting differently affected on Cu incorporation. (iii) The films sintered at 500 and 600 °C (1% at. Cu incorporation) yield maximum photocurrent and can be used as efficient photoelctrode for photosplitting of water. The effect can be attributed to better optical absorption and decreased electrical resistivity of samples.

Acknowledgements Financial assistance from DAE-BRNS, Govt. of India, in form of R&D project sanctioned to RS is gratefully acknowledged. VS thanks the same agency for the Junior Research Fellowship accorded to her under above project.

References

1. Fujishima A, Honda K (1972) Nature 238:37
2. Chen Z, Jaramillo TF, Deutsch TG, Kleiman-Shwarsctien A, Forman AJ, Gaillard N, Garland R, Takanabe K, Heske C, Sunkara M, Mcfarland EW, Domen K, Miller EL, Turner JA, Dinh HN (2010) J Mater Res 25:3
3. Chaudhary YS, Agrawal A, Shrivastav R, Satsangi VR, Dass S (2004) Int J Hydrogen Energy 29:131
4. Satsangi VR, Kumari S, Singh AP, Shrivastav R, Dass S (2008) Int J Hydrogen Energy 33:312
5. Chaudhary YS, Agrawal M, Kumari S, Shrivastav A, Shrivastav R, Satsangi VR, Dass S (2004) Ind J Phys 78A:229
6. Gupta M, Sharma V, Shrivastava J, Solanki A, Singh AP, Satsangi VR, Dass S, Shrivastav R (2009) Bull Mater Sci 32(1):23
7. Sharma V, Kumar P, Shrivastava J, Solanki A, Satsangi VR, Dass S, Shrivastav R (2011) Int J Hydrogen Energy (In press)
8. Pankove JI (1975) Optical progress in semiconductors. Dover Publications, New York
9. Krol RVD, Liang Y, Schoonman J (2008) J Mater Chem 18:2311
10. Chu D, Masuda Y, Ohji T, Kato K (2010) Langmuir 26:2811
11. Yun SY, Cha Gi-b, Kwon Y, Cho S, Soon SC, Hong (2004) J Magn Magn Mater 272–276:E1563
12. Gruzintsev AN, Volkov VT, Yakimov EE (2003) Semiconductors 37:259
13. Al-Hilli S, Willander M (2009) Sensors 9:7445
14. Satoh H, Kudoh K, Yoshio K, Yamazaki T, Matsuki K, Shimono I, Sakagamt N, Onodera A (2001) Ferroelectrics 264:139
15. Bahsi ZB, Oral AY (2007) Opt Mater 29672:678
16. Zhang J, Cong L, Wan H, Wang T (2009) Appl Surf Sci 255:3530
17. Yao B, Guan LX, Xing GZ, Zhang ZZ, Li BH, Wei ZP, Wang XH, Cong CX, Xie YP, Lu YM, Shen DZ (2007) J Lumin 122–123:191
18. Ohyama M, Kouzuka H, Yoko T (1997) Thin Solid Films 306:78
19. Shokuhfar A, Samei J, Kandjani AE, Vaezi MR (2008) Defect Diffus forum 273–276:626
20. Ozturk S, Tasaltin N, Kilinc N, Ozturk ZZ (2009) J Optoelectron Biomed Mater 1:15
21. Farley NRS, Staddon CR, Zhao L, Edmonds KW, Gallagher BL, Gregory DH (2004) J Mater Chem 14:1087
22. Kathirvel P, Manoharan D, Mohan SM, Kumar S (2009) J Optoelectron Biomed Mater 1:25
23. Ray SC (2001) J Sol Energy Mater Sol Cells 68:307
24. Shinar R, Kennedy JH (1982) J Sol Energy Mater Sol Cells 6:323
25. Ashrafi A, Jagdish CJ (2007) Appl Phys 102:071101
26. Zhou WJ, Liu G (2009) J Alloys Compd 487:545
27. Maruyama T (1998) Jpn J Appl Phys 37:4099
28. Wang J, Sallet V, Jomard F, Rego AM, Elamurugu E, Martins R, Fortunato E (2007) Thin Solid Films 515:8785
29. Musat V, Rego AM, Monteiro R, Fortunato E (2008) Thin Solid Films 516:1512

30. Huybrechts B, Ishizaki K, Tokata M (1993) J Eur Ceram Soc 11:395
31. Kim SK, Jeong SY, Cho CR (2003) Appl Phys Lett 82:562
32. Bao DH, Gu HS, Kuang AX (1998) Thin Solid Films 312:37
33. Caglar M, Ilican S, Caglar Y, Yakuphanoglu F (2009) Appl Surf Sci 255:4491
34. Atzmuller R, Schaak G, Becker CR (1996) Phys Rev B 54:16907
35. Gao F, Naik SP, Sasaki Y, Okubo T (2006) Thin Solid Films 495:68
36. Kao MC, Chen HZ, Young SL, Kung CY, Lin CC, Lai JZ (2009) J Supercond Nov Magn 23:897
37. Parthasarathy M, Ramgir NS, Sathe BR, Mulla IS, Pillai VK (2007) J Phys Chem C 111:13092